Vietnam Journal of Mechanics, VAST, Vol. 43, No. 4 (2021), pp. 347 – 357
DOI: https://doi.org/10.15625/0866-7136/16393

A NUMERICAL STUDY OF THE SOLIDIFICATION PROCESS OF A RETRACTING FLUID FILAMENT

Binh D. Pham[1,2], Truong V. Vu[1,*], Lien V. T. Nguyen[2], Cuong T. Nguyen[1], Hoe D. Nguyen[1,2], Vinh T. Nguyen[1,2], Hung V. Vu[1,3]

[1]*Faculty of Vehicle and Energy Engineering, Phenikaa University, Hanoi, Vietnam*
[2]*Graduate University of Science and Technology, Vietnam Academy of Science and Technology, 18 Hoang Quoc Viet street, Cau Giay district, Hanoi, Vietnam*
[3]*School of Transportation Engineering, Hanoi University of Science and Technology, 01 Dai Co Viet street, Hai Ba Trung district, Hanoi, Vietnam*
[*]E-mail: truong.vuvan@phenikaa-uni.edu.vn

Received: 16 August 2021 / Published online: 01 November 2021

Abstract. In this study, the retraction and solidification of a fluid filament are studied by a front-tracking method/finite difference scheme. The interface between two phases is handled by connected points (Lagrangian grid), which move on a fixed grid domain (Eulerian grid). The Navier-Stokes and energy equations are solved to simulate the problem. Initially, the fluid filament has a shape as half of a cylindrical capsule contact with a cold flat surface. We consider the effect of the aspect ratio (Ar) on the solidification of the fluid filament. It is found that an increase in the aspect ratio (Ar) in the range of 2 – 14 causes the retraction length to increase. The rate of the solidification of a fluid filament decreases when the Ar ratio increases. The solidification time, the solidification height and the tip angle of the fluid filament under the influence of the aspect ratio are also considered. After complete solidification, a small protrusion on the top of the solidified fluid filament is found.

Keywords: front-tracking method, fluid filament, cold flat surface.

1. INTRODUCTION

There are a lot of industrial processes such as manufacturing drugs [1], food production processes [2, 3] related to solidification of fluid drops. In addition, solidification of fluid drops can be seen in life such as in the hail phenomenon, the cooling types of equipment and the blades of aircraft and wind turbines [4, 5]. Huang et al. [6] did experiments on water drops placed on a cold plate. The authors tracked the solidification process of the water drops by varying the wetting angle in the range of 97.2° – 154.9°. With similar experiments, Pan et al. [7] considered the solidification of water drops laid on a cold plate surface or an inclined surface with a tilt angle of 30°. The authors monitored the water

drops with the variable wetting angle in the range of 77° – 145°. Zhang et al. [8] and Ju et al. [9] did experiments on solidification of water drops on different curved surfaces. Investigating the growth angle, Satunkin [10] used molten Silicon, Germanium and Indium antimonide solidified on a cold plate. The author found that the drop shape of these materials after complete solidification is different because their growth angles are not the same. Numerically, Schultz et al. [11] investigated a water droplet solidified on a cold plate with a single triple point and growth angle assumed constant. Virozub et al. [12] estimated and verified the growth angle of molten drops with a thermal model of the materials e.g., water, silicon and germanium. Vu et al. [13] used a front-tracking method to simulate the solidification of liquid drops on a cold plate. Some works about the solidification of simple liquid drops can be found in [14–19]. These studies have only considered the solidification of static drops. Considering the solidification of a break-up drop under gravity force, Vu et al. [20, 21] performed simulations of solidification of a drop stretched by a gravity force. However, all these studies have not considered and taken into account the solidification process of a retracting fluid filament.

Considering the retraction of a fluid filament, Driessen et al. [22] studied the stabilization of a viscous liquid filament. The authors found that each value of the aspect ratio, Ohnesorge number and the relative perturbation amplitude leads to merge into a single droplet or breakup into the sub-droplets. Dziedzic et al. [23] monitored the transition from a non-breakup to a breakup of a fluid filament with the effect of substrates and parameters such as Ohnesorge number (Oh) and aspect ratio (Ar). Recently, the retraction of a compound fluid filament leading to break up into sub-droplets and non-breakup was studied by Ho et al. [24]. The inner aspect ratio (Ar_i) in the range of 5 – 30 and outer aspect ratio (Ar_o) in the range of 7.5 – 30 was considered. Many works about the retraction of a fluid filament can be found in [24–29]. However, these works have not considered the solidification process.

Although there are many applications in which solidification can appear along with the retraction process of fluid filaments [30–32], the solidification process of a liquid filament has not considered in detail yet. This study aims to solve this missing gap. The paper includes 4 sections. Section 1 introduces the aim of this study. Section 2 presents the numerical model and method. Section 3 provide a grid resolution to simulate the problem. Section 4 shows the numerical results and discussion. Finally, Section 5 provides the conclusions.

2. NUMERICAL MODEL AND METHOD

This paper considers the retraction and solidification of a fluid filament contacting on a cold flat surface (Fig. 1). Initially, the fluid filament is assumed to a half of a symmetrical capsule shape and its bottom contacts a cold flat surface (Fig. 1(a)). The initial length of a fluid filament is L_0 and its initial radius is R. In order to save the computational resources and time, the fluid filament is assumed axisymmetric and simulated in a cylindrical coordinate system. Fig. 1(b) describes a computational domain of the fluid filament with the solidification process. The fluid and gas are assumed as incompressible, immiscible and Newtonian fluids. Viscosity (μ), density (ρ), heat capacity (C_p) and thermal conductivity (k) in each phase are assumed as constant properties. The governing equations are given as

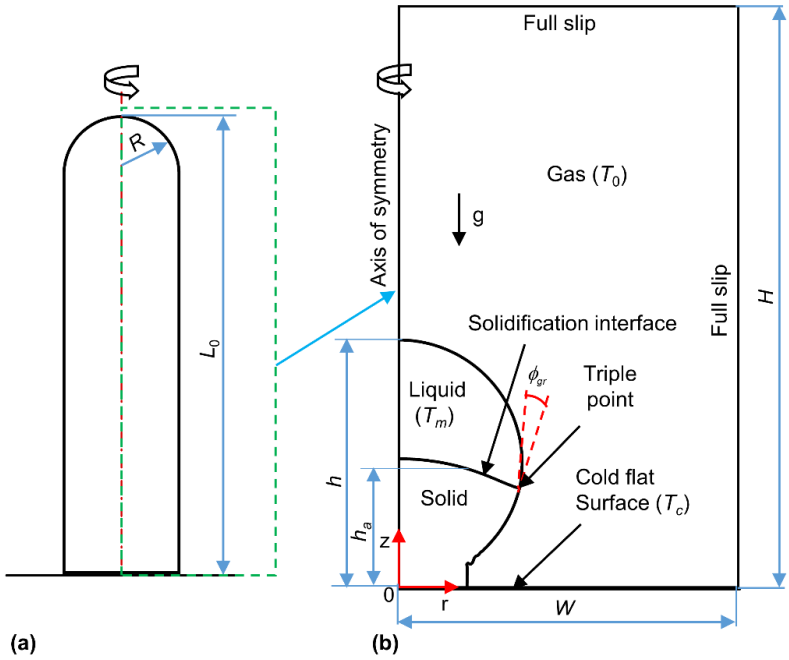

Fig. 1. A numerical configuration of the solidification of a fluid filament.
(a) An initial fluid filament contacts a cold flat surface that leads to solidification.
(b) The computational domain for the problem

$$\frac{\partial \rho \mathbf{u}}{\partial t} + \nabla \rho \mathbf{u} = -\nabla p + \nabla \left[\mu \left(\nabla \mathbf{u} + \nabla \mathbf{u}^T \right) \right] + \int_f \sigma \kappa \left(\mathbf{x} - \mathbf{x}_f \right) \mathbf{n}_f \mathrm{d}S + \rho \mathbf{f} + \rho \mathbf{g}, \tag{1}$$

$$\frac{\partial \rho C_p T}{\partial t} + \nabla \rho C_p T \mathbf{u} = \nabla \left(k \nabla T \right) + \int_f \dot{q} \delta \left(\mathbf{x} - \mathbf{x}_f \right) \mathrm{d}S, \tag{2}$$

$$\nabla \cdot \mathbf{u} = \frac{\rho_l - \rho_s}{L_h \rho_l \rho_s} \int_f \dot{q} \delta \left(\mathbf{x} - \mathbf{x}_f \right) \mathrm{d}S, \tag{3}$$

$$\dot{q} = k_s \frac{\partial T}{\partial n} \Big)_s - k_l \frac{\partial T}{\partial n} \Big)_l, \tag{4}$$

where, $\mathbf{u}$ and p stand for the velocity vector and pressure, respectively. t and superscript T are the time and the transpose. σ and κ correspond to the interfacial tension coefficient and twice mean curvature. $\mathbf{x}$ is the position vector, subscript f represents the interface, $\mathbf{n}$ is the unit normal vector to the interface. δ is the denotation of the Dirac delta function and its value is 1 at the interface $\mathbf{x}_f$ and 0 at the other positions. $\mathbf{f}$ is the external force and used to apply the no-slip condition on the solid interface [33, 34], $\mathbf{g}$ is the gravity acceleration, $\dot{q}$ is the denotation of thermal flux at the solidification interface. L_h is the

latent heat. T is the temperature. The dimensionless parameters used in this paper are

$$Pr = \frac{C_{pl}\mu_l}{k_l}, \quad St = \frac{C_{pl}(T_m - T_c)}{L_h}, \quad Bo = \frac{\rho_l g R^2}{\sigma}, \quad Oh = \frac{\mu_l}{\sqrt{\rho_l R \sigma}}, \tag{5}$$

$$\theta_0 = \frac{T_0 - T_c}{T_m - T_c}, \quad \rho_{sl} = \frac{\rho_s}{\rho_l}, \quad \rho_{gl} = \frac{\rho_g}{\rho_l}, \quad \mu_{gl} = \frac{\mu_g}{\mu_l}, \quad Ar = \frac{L_0}{R}, \tag{6}$$

$$k_{sl} = \frac{k_s}{k_l}, \quad k_{gl} = \frac{k_g}{k_l}, \quad C_{psl} = \frac{C_{ps}}{C_{pl}}, \quad C_{pgl} = \frac{C_{pg}}{C_{pl}}, \tag{7}$$

where, Pr, St, Bo and Oh correspond to Prandtl, Stefan, Bond and Ohnesorge numbers. θ_0 is the denotation of the initial normalized temperature. Because we consider small fluid filaments, the effect of gravity force plays minor role [23, 24, 35, 36]. Therefore, in this study, we ignore the effect of gravity, i.e., $Bo = 0$. The ratios of the properties of the phases are ρ_{sl}, ρ_{gl} – density ratios; μ_{gl} – viscosity ratio; k_{sl}, k_{gl} – thermal conductivity ratios, C_{psl}, C_{pgl} – heat capacity ratios. Subscripts s, l and g stand for solid, liquid and gas phases, respectively. The aspect ratio is denoted by Ar. With $\tau_c = \rho_l C_{pl} R^2 / k_l$, the non-dimensional time is $\tau = t/\tau_c$.

The method used in this study is a front-tracking method [37–39]. This is one of the powerful methods to solve a multiphase problem. The interfaces among the phases are modeled by the chain of the Lagrangian points ($\mathbf{x}_f$) laid on a fixed grid (Eulerian grid) which is a staggered grid with uniformly distributed grid points.

Thanks to the interfacial points ($\mathbf{x}_f$), we can compute the interfacial forces acting on the interfaces and thus build the indicator functions to specify the properties of phases. Here, we use two indicators I_1 and I_2 reconstructed from the position of the interfaces. The value of each indicator is 1 in a phase and 0 in the other. With φ standing for the properties of phases such as the density (ρ), the viscosity (μ), the thermal conductivity (k), and the heat capacity (C_p), we have [40]

$$\varphi = \left[\varphi_s I_1 + \varphi_l \left(1 - I_1\right)\right] I_2 + \varphi_g \left(1 - I_2\right). \tag{8}$$

More details on our methods can be found in [38, 41].

3. GRID REFINEMENT

This method was carefully validated in our previous works [37]. Therefore, the validation of the method is not conducted here. We here only consider the grid refinement. The parameters are used as $Pr = 7, St = 0.1, Oh = 0.2, \theta_0 = 1, \rho_{sl} = 0.9, \rho_{gl} = 0.05, \mu_{gl} = 0.04, Ar = 3, k_{sl} = 4, k_{gl} = 0.05, C_{psl} = 0.5, C_{pgl} = 0.24$, and growth angle $\phi_{gr} = 0°$ along with the domain size W × H = 4R × 6R. Three grid resolutions are considered 128 × 192, 192 × 288 and 256 × 384. Fig. 2 shows grid convergence results of the different grid resolutions. We use the average solidification interface height (h_a) given as

$$h_a = \frac{\sum_{i=1}^{N_s} z_{si}}{N_s} \tag{9}$$

where z_{si} is the axial coordinate of the point i on the solidification interface and N_s is the number of points on the solidification interface. Figs. 2(a) and 2(b) correspond to the fluid filament in the solidification process and the average solidification interface height (h_a) of three grid resolutions. Accordingly, we see that the results of the grid resolutions 192 × 288 and 256 × 384 are almost identical and grid resolution 128 × 192 has some difference compared to the other grid resolutions. Specifically, in Fig. 2(b), the mean error of the solidification interface height (h_a) of the grid resolution 128 × 192 compared with the grid resolution 256 × 384 is 0.623%. Meanwhile, the mean error of the grid resolution 192 × 288 is 0.208% compared to the grid resolution 256 × 384. To save computation time and still ensure accuracy, the grid resolution 192 × 288 is chosen to simulate this problem.

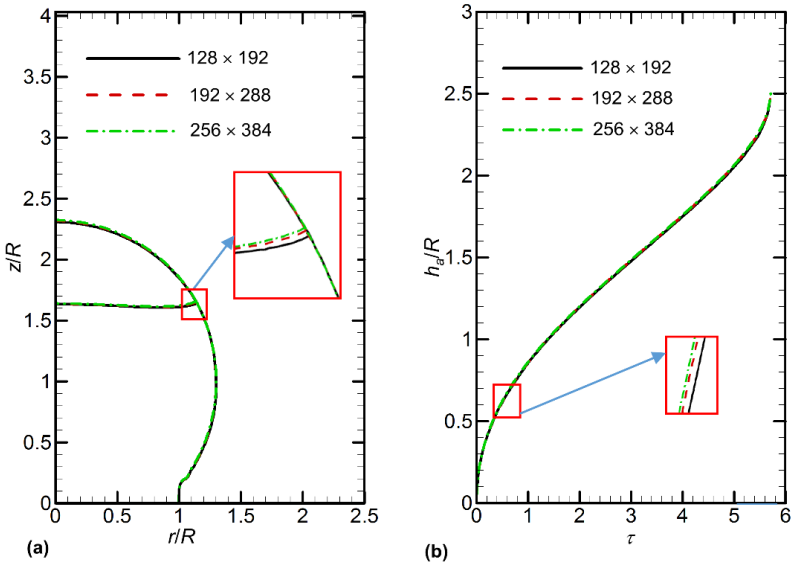

Fig. 2. Grid refinement. (a) The shape of fluid filaments in the solidification process with different grid resolutions. (b) The average solidification interface height (h_a) of the fluid filaments over time with the different grid resolutions

4. RESULTS AND DISCUSSION

The solidification process of the fluid filaments $Ar = 4$ and $Ar = 8$ is presented in Fig. 3. The parameters are $Pr = 7, St = 0.1, Oh = 0.2, \theta_0 = 1, \rho_{sl} = 0.9, \rho_{gl} = 0.05, \mu_{gl} = 0.04, k_{sl} = 4, k_{gl} = 0.05, C_{psl} = 0.5, C_{pgl} = 0.24$, and $\phi_{gr} = 0°$. Fig. 3(a) shows the fluid filaments at the initial time ($\tau = 0$). At $\tau = 0.15$ (Fig. 3(b)), the left fluid filament ($Ar = 4$) has finished its retraction and is in the process of oscillation presented by the counter-clockwise velocity field. Meanwhile, the right fluid filament ($Ar = 8$) is in the process of retraction described by its velocity field. This indicates the process of retraction of the fluid filament $Ar = 4$ faster than that of the fluid filament $Ar = 8$. It is understandable that the fluid filament with $Ar = 4$ has a shorter retraction distance than the one with $Ar = 8$. Next is the process of stabilization and complete solidification. This process

takes the longest time. In this process, the fluid filaments no longer oscillate much except for the expansion of the phase change (because the density of the liquid phase is greater than that of the solid phase). Fig. 3(c) shows the solidification of the fluid filament in the stabilization and complete solidification process at τ = 5.1. It can be seen that the solidification interface height of the fluid filament with $Ar = 4$ is higher than that with $Ar = 8$. When the stabilization and complete solidification process ends, the fluid filaments are completely solidified (Fig. 3(d)). In Fig. 3(d), the fluid filament with $Ar = 4$ completes the solidification earlier than the fluid filament with $Ar = 8$ ($\tau_s = 8.49$ compared to $\tau_s = 21.45$) and the solidification height of the fluid filament with $Ar = 8$ is higher than that of the fluid filament with $Ar = 4$. This is understandable that because the height of the fluid filament with $Ar = 4$ is lower than that of the fluid filament with $Ar = 8$. Therefore, the volume of the fluid filament with $Ar = 4$ is smaller than that of the fluid filament with $Ar = 8$, leading to the left fluid filament ($Ar = 4$) finishing the solidification first and its solidification height lower than the right fluid filament ($Ar = 8$). Because of the expansion of the volume upon solidification, the solidified fluid filament has a small protrusion at its top like the solidification of simple droplets [16] with a tip angle denoted by α_t (see in Fig. 3(d)).

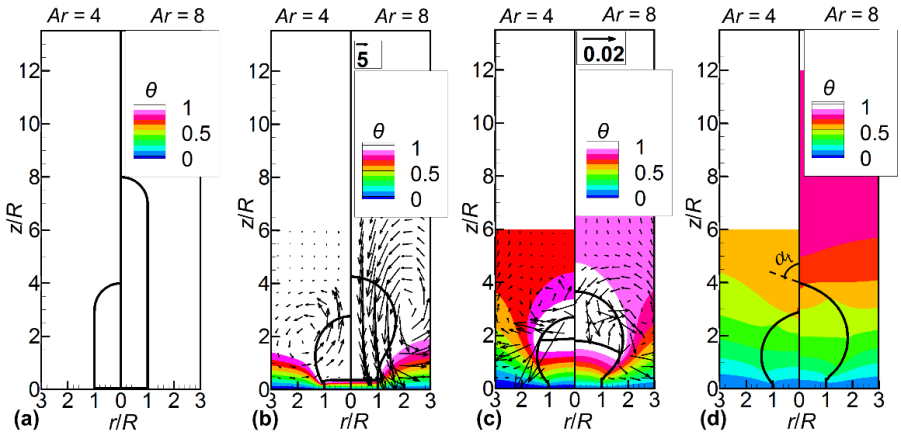

Fig. 3. The solidification process of fluid filaments $Ar = 4$ (left) and $Ar = 8$ (right) with the normalized temperature field $\theta = (T - T_c)/(T_m - T_c)$. (a) The fluid filaments at the initial time ($\tau = 0$). (b) The fluid filaments at $\tau = 0.15$. (c) The fluid filament at $\tau = 5.1$. (d) The fluid filament $Ar = 4$ is complete solidification at $\tau = \tau_s = 8.49$ and the fluid filament $Ar = 8$ solidifies completely at $\tau = \tau_s = 21.45$. In (b) and (c), the velocity field is normalized by $U_c = k_l/(\rho_l C_{pl} R)$

4.1. Retraction of fluid filaments during the solidification with various aspect ratios

Fig. 4 illustrates the variation of the retraction length ($h_0 - h$) (h_0 and h defined below) with various aspect ratios (Ar) in the range of 2 – 14. The other parameters are kept constant such as $Pr = 7, St = 0.1, Oh = 0.2, \theta_0 = 1, \rho_{sl} = 0.9, \rho_{gl} = 0.05, \mu_{gl} = 0.04, k_{sl} = 4, k_{gl} = 0.05, C_{psl} = 0.5, C_{pgl} = 0.24$, and $\phi_{gr} = 0°$. Considering the solidification of the fluid filaments with $Ar = 6$ and $Ar = 10$ at $\tau = 3$ in Fig. 4(a), we see that although the height of the left fluid filament ($Ar = 6$) is lower than that of the right fluid

filament ($Ar = 10$), the solidification front height is almost identical at τ = 3. With the initial height of the fluid filaments ($h_0 = L_0$) and the height of the fluid filaments (h) at τ, Fig. 4(b) shows the retraction length corresponding to the aspect ratio (Ar) in the range of 2 – 14 over time (τ). In the initial stage, the retraction length of the fluid filaments increases sharply. Increasing the Ar ratio increases the retraction length and the time for the initial stage. Interestingly, in this stage, the rate of retraction, i.e., the speed of retraction, is independent of the variation of the Ar ratio. The next stage is oscillation after the filament retracts to a certain length. In this stage, the oscillation of the fluid filaments is damped overtime. The lower the aspect ratio (Ar), the shorter the oscillation period. It is due to the inertia force of the fluid filaments when they retract. The smaller the aspect ratio (Ar), the smaller the retraction time and the smaller the inertia force. The final stage is stabilization and complete solidification. In this stage, the fluid filaments keeps solidifying until complete solidification. The height of the fluid filaments is slightly increased because of the expansion of volume. Therefore, the final retraction length of the fluid filaments decreases a little.

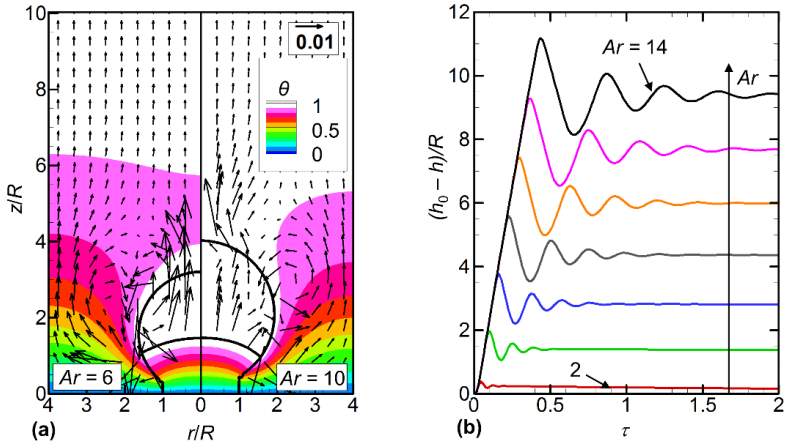

Fig. 4. Retraction length of fluid filaments in solidification. (a) The fluid filaments in the solidification process with $Ar = 6$ (left) and $Ar = 10$ (right) along with the normalized temperature field θ at $\tau = 3$. (b) The retraction length of fluid filaments over time with the aspect ratio (Ar) in the range of 2 – 14. In (a), the velocity field is normalized by U_c and the arrow in (b) is the increase of the aspect ratio (Ar)

4.2. Average solidification interface height, solidification time, solidification height and tip angle with various aspect ratios

Fig. 5 describes the average solidification interface height (h_a), the solidification time (τ_s), the solidification height (h_s) and the tip angle (α_t) with various aspect ratios (Ar) in the range of 2 – 14. The other parameters are the same as those in the previous figure. Fig. 5(a) the shows that when the aspect ratio (Ar) increases, the height of the solidified fluid filament ($h_s = h_a(\tau = \tau_s)$) increases. This can be explained that an increasing aspect ratio (Ar) leads to an increase in the volume of fluid filaments. Interestingly, at the

same time $\tau > 2.0$, the smaller the aspect ratio (Ar), the higher the average solidification interface height (h_a). It means that the rate of solidification of the fluid filaments increases when the aspect ratio (Ar) decreases. This is because a fluid filament with a small aspect ratio (Ar) has a smaller thermal boundary layer around the fluid filament than that with a large aspect ratio (Ar) (see in Fig. 4(a)). This causes the solidification interface near the triple point of the fluid filament with a small aspect ratio (Ar) to move faster than that with a large aspect ratio (Ar) (see in Fig. 3(c)). In addition, Fig. 5(a) also illustrates that the solidification time (τ_s) increases when the aspect ratio (Ar) increases. For further demonstration, Fig. 5(b) shows the solidification time (τ_s), solidification height (h_s) and tip angle (α_t) with the aspect ratio (Ar) varying in the range of 2 – 14. We see that the solidification time (τ_s) and solidification height (h_s) increase sharply when the aspect ratio (Ar) increases in the range of 2 – 14. In contrast, the tip angle (α_t) is almost unchanged ($\alpha_t \approx 76.49°$) with the aspect ratio (Ar) varying in the range of 2 – 14. In other words, varying the aspect ratio (Ar) does not affect the tip angle [42, 43].

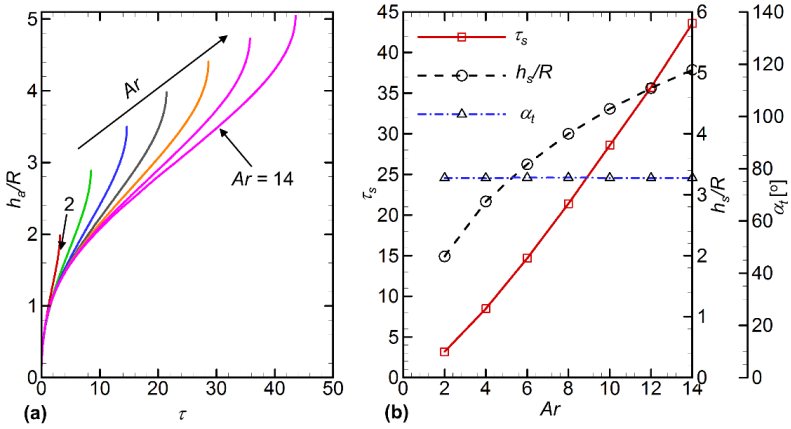

Fig. 5. (a) The average solidification interface height (h_a) over time (τ) with the various aspect ratios (Ar) in the range of 2 - 14. (b) The solidification time (τ_s), solidification height (h_s) and tip angle (α_t) of the fluid filaments with the various aspect ratios (Ar) in the range of 2 – 14. The arrow in (a) shows the increase of Ar. In (b) the solidification time increases with the aspect ratio (Ar) by $\tau_s \approx 3.3872Ar - 4.8451$ and the solidification height increases with the aspect ratio (Ar) by $h_s/R \approx 1.5807\ln(Ar) + 0.7775$

5. CONCLUSIONS

We have presented the solidification of fluid filaments retracting under the influence of the various aspect ratios (Ar) in the range of 2 – 14 by using the front-tracking method. Like the solidification of simple droplets on a cold plate, the small protrusion on the top of solidified fluid filament has appeared after complete retraction and solidification. The solidification process can be divided into three stages. Stage 1 is the retraction process – this process is very fast. Stage 2 is the oscillation process – in this process, the fluid

filament is in damped oscillation. Finally, stage 3 is the process of stabilization and complete solidification – the height of fluid filament increases a bit over time in this process. Varying the aspect ratio (Ar) in the range of 2 – 14, the retraction length ($h_0 - h$) increases when the Ar ratio increases. The retraction and oscillation stages take place longer when the aspect ratio (Ar) increases. An increase in the aspect ratio leads to an increase in the height of the solidified fluid filament but a decrease in the solidification rate. In addition, the solidification time increases with the aspect ratio (Ar). Meanwhile, varying the aspect ratio (Ar) in the range of 2 – 14 has no effect on the tip angle (α_t).

ACKNOWLEDGEMENTS

This research is funded by Vietnam National Foundation for Science and Technology Development (NAFOSTED) under grant number 107.03-2019.307. Binh D. Pham was funded by Vingroup Joint Stock Company and supported by the Domestic Master/ PhD Scholarship Programme of Vingroup Innovation Foundation (VINIF), Vingroup Big Data Institute (VINBIGDATA), code VINIF.2020.TS.140.

REFERENCES

[1] D. J. McClements. Advances in fabrication of emulsions with enhanced functionality using structural design principles. *Current Opinion in Colloid & Interface Science*, **17**, (2012), pp. 235–245. https://doi.org/10.1016/j.cocis.2012.06.002.

[2] A. A. Maan, K. Schroën, and R. Boom. Spontaneous droplet formation techniques for monodisperse emulsions preparation – perspectives for food applications. *Journal of Food Engineering*, **107**, (2011), pp. 334–346. https://doi.org/10.1016/j.jfoodeng.2011.07.008.

[3] G. Muschiolik. Multiple emulsions for food use. *Current Opinion in Colloid & Interface Science*, **12**, (2007), pp. 213–220. https://doi.org/10.1016/j.cocis.2007.07.006.

[4] W. J. Jasinski, S. C. Noe, M. S. Selig, and M. B. Bragg. Wind turbine performance under icing conditions. *Journal of Solar Energy Engineering*, **120**, (1998), pp. 60–65. https://doi.org/10.1115/1.2888048.

[5] Y. Cao, Z. Wu, Y. Su, and Z. Xu. Aircraft flight characteristics in icing conditions. *Progress in Aerospace Sciences*, **74**, (2015), pp. 62–80. https://doi.org/10.1016/j.paerosci.2014.12.001.

[6] L. Huang, Z. Liu, Y. Liu, Y. Gou, and L. Wang. Effect of contact angle on water droplet freezing process on a cold flat surface. *Experimental Thermal and Fluid Science*, **40**, (2012), pp. 74–80. https://doi.org/10.1016/j.expthermflusci.2012.02.002.

[7] Y. Pan, K. Shi, X. Duan, and G. F. Naterer. Experimental investigation of water droplet impact and freezing on micropatterned stainless steel surfaces with varying wettabilities. *International Journal of Heat and Mass Transfer*, **129**, (2019), pp. 953–964. https://doi.org/10.1016/j.ijheatmasstransfer.2018.10.032.

[8] H. Zhang, Z. Jin, M. Jiao, and Z. Yang. Experimental investigation of the impact and freezing processes of a water droplet on different cold concave surfaces. *International Journal of Thermal Sciences*, **132**, (2018), pp. 498–508. https://doi.org/10.1016/j.ijthermalsci.2018.06.032.

[9] J. Ju, Z. Jin, H. Zhang, Z. Yang, and J. Zhang. The impact and freezing processes of a water droplet on different cold spherical surfaces. *Experimental Thermal and Fluid Science*, **96**, (2018), pp. 430–440. https://doi.org/10.1016/j.expthermflusci.2018.03.037.

[10] G. A. Satunkin. Determination of growth angles, wetting angles, interfacial tensions and capillary constant values of melts. *Journal of Crystal Growth*, **255**, (2003), pp. 170–189. https://doi.org/10.1016/s0022-0248(03)01187-4.

[11] W. W. Schultz, M. G. Worster, and D. M. Anderson. Solidifying sessile water droplets. In *Interactive Dynamics of Convection and Solidification*, Springer, Dordrecht, (2001), pp. 209–226, https://doi.org/10.1007/978-94-015-9807-1_24.
[12] A. Virozub, I. G. Rasin, and S. Brandon. Revisiting the constant growth angle: Estimation and verification via rigorous thermal modeling. *Journal of Crystal Growth*, **310**, (2008), pp. 5416–5422. https://doi.org/10.1016/j.jcrysgro.2008.09.004.
[13] T. V. Vu, G. Tryggvason, S. Homma, and J. C. Wells. Numerical investigations of drop solidification on a cold plate in the presence of volume change. *International Journal of Multiphase Flow*, **76**, (2015), pp. 73–85. https://doi.org/10.1016/j.ijmultiphaseflow.2015.07.005.
[14] C. Zhang, H. Zhang, W. Fang, Y. Zhao, and C. Yang. Axisymmetric lattice Boltzmann model for simulating the freezing process of a sessile water droplet with volume change. *Physical Review E*, **101**, (2020). https://doi.org/10.1103/physreve.101.023314.
[15] H. Shetabivash, A. Dolatabadi, and M. Paraschivoiu. A multiple level-set approach for modelling containerless freezing process. *Journal of Computational Physics*, **415**, (2020). https://doi.org/10.1016/j.jcp.2020.109527.
[16] T. V. Vu and Q. H. Luu. Containerless solidification of a droplet under forced convection. *International Journal of Heat and Mass Transfer*, **143**, (2019). https://doi.org/10.1016/j.ijheatmasstransfer.2019.118498.
[17] T. V. Vu, C. T. Nguyen, and D. T. Khanh. Direct numerical study of a molten metal drop solidifying on a cold plate with different wettability. *Metals*, **8**, (2018). https://doi.org/10.3390/met8010047.
[18] V. N. Duy and T. V. Vu. A numerical study of a liquid drop solidifying on a vertical cold wall. *International Journal of Heat and Mass Transfer*, **127**, (2018), pp. 302–312. https://doi.org/10.1016/j.ijheatmasstransfer.2018.08.031.
[19] T. V. Vu. Fully resolved simulations of drop solidification under forced convection. *International Journal of Heat and Mass Transfer*, **122**, (2018), pp. 252–263. https://doi.org/10.1016/j.ijheatmasstransfer.2018.01.124.
[20] T. V. Vu, K. V. Dao, and B. D. Pham. Numerical simulation of the freezing process of a water drop attached to a cold plate. *Journal of Mechanical Science and Technology*, **32**, (2018), pp. 2119–2126. https://doi.org/10.1007/s12206-018-0421-4.
[21] T. V. Vu. Deformation and breakup of a pendant drop with solidification. *International Journal of Heat and Mass Transfer*, **122**, (2018), pp. 341–353. https://doi.org/10.1016/j.ijheatmasstransfer.2018.01.125.
[22] T. Driessen, R. Jeurissen, H. Wijshoff, F. Toschi, and D. Lohse. Stability of viscous long liquid filaments. *Physics of Fluids*, **25**, (2013). https://doi.org/10.1063/1.4811849.
[23] A. Dziedzic, M. Nakrani, B. Ezra, M. Syed, S. Popinet, and S. Afkhami. Breakup of finite-size liquid filaments: Transition from no-breakup to breakup including substrate effects⋆. *The European Physical Journal E*, **42**, (2019). https://doi.org/10.1140/epje/i2019-11785-y.
[24] N. X. Ho, T. V. Vu, V. T. Nguyen, C. T. Nguyen, and H. V. Vu. A numerical study of liquid compound filament contraction. *Physics of Fluids*, **33**, (2021). https://doi.org/10.1063/5.0040216.
[25] S. Hansen, G. W. M. Peters, and H. E. H. Meijer. The effect of surfactant on the stability of a fluid filament embedded in a viscous fluid. *Journal of Fluid Mechanics*, **382**, (1999), pp. 331–349. https://doi.org/10.1017/s0022112098003991.
[26] Y. Su, B. Palacios, and R. Zenit. Coiling of a viscoelastic fluid filament. *Physical Review Fluids*, **6**, (2021). https://doi.org/10.1103/physrevfluids.6.033303.
[27] X. Zhang. Dynamics of growth and breakup of viscous pendant drops into air. *Journal of Colloid and Interface Science*, **212**, (1999), pp. 107–122. https://doi.org/10.1006/jcis.1998.6047.

[28] T. V. Vu, S. Homma, J. C. Wells, H. Takakura, and G. Tryggvason. Numerical simulation of formation and breakup of a three-fluid compound jet. *Journal of Fluid Science and Technology*, **6**, (2), (2011), pp. 252–263. https://doi.org/10.1299/jfst.6.252.

[29] T. V. Vu, J. C. Wells, H. Takakura, S. Homma, and G. Tryggvason. Numerical calculations of pattern formation of compound drops detaching from a compound jet in a co-flowing immiscible fluid. *Journal of Chemical Engineering of Japan*, **45**, (9), (2012), pp. 721–726. https://doi.org/10.1252/jcej.11we256.

[30] Cults. *Identify and correct 3D printing problems*.

[31] K. Paraskevoudis, P. Karayannis, and E. P. Koumoulos. Real-time 3D printing remote defect detection (stringing) with computer vision and artificial intelligence. *Processes*, **8**, (2020). https://doi.org/10.3390/pr8111464.

[32] W. Oropallo and L. A. Piegl. Ten challenges in 3D printing. *Engineering with Computers*, **32**, (2015), pp. 135–148. https://doi.org/10.1007/s00366-015-0407-0.

[33] T. V. Vu, A. V. Truong, N. T. B. Hoang, and D. K. Tran. Numerical investigations of solidification around a circular cylinder under forced convection. *Journal of Mechanical Science and Technology*, **30**, (2016), pp. 5019–5028. https://doi.org/10.1007/s12206-016-1021-9.

[34] T. V. Vu and J. C. Wells. Numerical simulations of solidification around two tandemly-arranged circular cylinders under forced convection. *International Journal of Multiphase Flow*, **89**, (2017), pp. 331–344. https://doi.org/10.1016/j.ijmultiphaseflow.2016.11.007.

[35] T. V. Vu, L. V. Vu, B. D. Pham, and Q. H. Luu. Numerical investigation of dynamic behavior of a compound drop in shear flow. *Journal of Mechanical Science and Technology*, **32**, (2018), pp. 2111–2117. https://doi.org/10.1007/s12206-018-0420-5.

[36] B. D. Pham, T. V. Vu, C. T. Nguyen, H. D. Nguyen, and V. T. Nguyen. Numerical study of collision modes of multi-core compound droplets in simple shear flow. *Journal of Mechanical Science and Technology*, **34**, (2020), pp. 2055–2066. https://doi.org/10.1007/s12206-020-0427-6.

[37] N. X. Ho, T. V. Vu, and B. D. Pham. A numerical study of a liquid compound drop solidifying on a horizontal surface. *International Journal of Heat and Mass Transfer*, **165**, (2021). https://doi.org/10.1016/j.ijheatmasstransfer.2020.120713.

[38] G. Tryggvason, B. Bunner, A. Esmaeeli, D. Juric, N. Al-Rawahi, W. Tauber, J. Han, S. Nas, and Y.-J. Jan. A front-tracking method for the computations of multiphase flow. *Journal of Computational Physics*, **169**, (2001), pp. 708–759. https://doi.org/10.1006/jcph.2001.6726.

[39] T. V. Vu, G. Tryggvason, S. Homma, J. C. Wells, and H. Takakura. A front-tracking method for three-phase computations of solidification with volume change. *Journal of Chemical Engineering of Japan*, **46**, (11), (2013), pp. 726–731. https://doi.org/10.1252/jcej.13we169.

[40] T.-V. Vu, T. V. Vu, C. T. Nguyen, and P. H. Pham. Deformation and breakup of a double-core compound droplet in an axisymmetric channel. *International Journal of Heat and Mass Transfer*, **135**, (2019), pp. 796–810. https://doi.org/10.1016/j.ijheatmasstransfer.2019.02.032.

[41] T. V. Vu. Three-phase computation of solidification in an open horizontal circular cylinder. *International Journal of Heat and Mass Transfer*, **111**, (2017), pp. 398–409. https://doi.org/10.1016/j.ijheatmasstransfer.2017.04.011.

[42] A. G. Marín, O. R. Enríquez, P. Brunet, P. Colinet, and J. H. Snoeijer. Universality of tip singularity formation in freezing water drops. *Physical Review Letters*, **113**, (2014). https://doi.org/10.1103/physrevlett.113.054301.

[43] X. Zhang, X. Wu, and J. Min. Freezing and melting of a sessile water droplet on a horizontal cold plate. *Experimental Thermal and Fluid Science*, **88**, (2017), pp. 1–7. https://doi.org/10.1016/j.expthermflusci.2017.05.009.